

Spin-orbit bi-colour modulation and analysis of structured light in a nonlinear optics experiment

Kiki Dekkers,^{1,†} Mwezi Koni,^{2,†} Vagharshak Hakobyan,³ Sachleen Singh,²
Jonathan Leach,¹ Etienne Brasselet,³ Isaac Nape² and Andrew Forbes^{2,*}

¹School of Engineering and Physical Sciences, Heriot-Watt University, Edinburgh, UK

²School of Physics, University of Witwatersrand, Johannesburg, South Africa

³University of Bordeaux, CNRS, Laboratoire Ondes et Matière d'Aquitaine, Talence, France

[†] These authors contributed equally to the work

* andrew.forbes@wits.ac.za

Here we propose the use of an adjustable liquid crystal spin-orbit device to shape and detect bi-colour structured light in a nonlinear optics framework. The spin-orbit device has an inhomogeneous optical axis orientation and birefringence, allowing it to modulate two wavelengths of light with pre-selected transmission functions by simply tuning a voltage. We combine this bi-colour functionality in a nonlinear optical experiment by employing three-wave mixing in a periodically poled crystal to show how the combined effect of linear spin-orbit transformation rules and nonlinear selection rules gives rise to novel approaches for light to modulate light, and light to unravel light. We show that the roles of the nonlinear crystal and spin-orbit device can be switched to either characterise the device with known light, or unravel unknown light with the device. This synergy between spin-orbit and nonlinear optics offers a novel paradigm where light manipulates and reveals its own structure across spectral domains.

I. INTRODUCTION

Light can be tailored in various degrees of freedom, so-called structured light [1], mostly with a linear optical toolkit such as spatial light modulators [2] and metasurfaces [3], giving rise to many exciting new fields and applications [4, 5]. Recently, the focus has shifted towards nonlinear control of structured light [6, 7], beyond just frequency conversion and towards new applications that include high-dimensional quantum [8, 9] and classical communication [10], real-time error correction [11], holography [12, 13] and new paradigms [14–17]. A modern trend is to mix degrees of freedom to create new forms of light, for instance, optical topologies [18] and spatiotemporal light [19], as well as emulating quantum states by nonseparable states of light [20].

A common route to generate and analyse structured light has been to couple polarisation and orbital angular momentum (OAM), with spin-orbit optical devices playing a central role in both the creation and detection of such states [21–25]. These devices have traditionally operated in linear optics and at a single wavelength. Yet, combining wavelength, polarisation, and OAM degrees of freedom is known to offer enhanced functionality and richer light–matter interactions [26, 27].

Here we use a spin-orbit liquid crystal device that can work for two wavelengths simultaneously, with the efficiency controlled by an applied voltage, allowing the tailoring of superposition of wavelength, polarisation, and OAM states simultaneously. The bi-colour behaviour lends itself to nonlinear creation and detection of structured light, which we demonstrate by characterising the modal properties of light in a quadratic nonlinear optical process, with access to both wavelengths while only measuring in the more easily detectable output wavelength. The device can be positioned either before or after the nonlinear stage, enabling two complementary modes of modulation—each shaping the detection of the light’s internal structure. This interplay of multi-degree-of-freedom control with bi-colour spin-orbit coupling in a nonlinear context suggests novel routes for advanced manipulation and decoding of structured light beyond bi-colour spin-orbit-based imaging applications [28, 29].

II. SPIN-ORBIT DEVICE AND NONLINEAR INTERACTION STAGES

The spin-orbit device, illustrated in Figs. 1(a) and 1(b), consists of a nematic liquid crystal (LC) cell combined with a cylindrical ring magnet (height: 6 mm, outer diameter: 8 mm, inner diameter: 4 mm) placed at a distance $d \simeq 2$ mm from the LC cell (EHC Co. Ltd., Japan) having a thickness of $L = 10 \pm 0.5 \mu\text{m}$ and is equipped with indium-tin-oxide electrodes for voltage control. Both confining glass substrates impose homeotropic anchoring, ensuring a uniform initial molecular alignment along the optical axis (z -direction). The cell is filled with the nematic mixture 1859A (MUT, Poland), which exhibits a birefringence of $\Delta n \simeq 0.229$ at a wavelength of $\lambda = 589$ nm and a negative dielectric

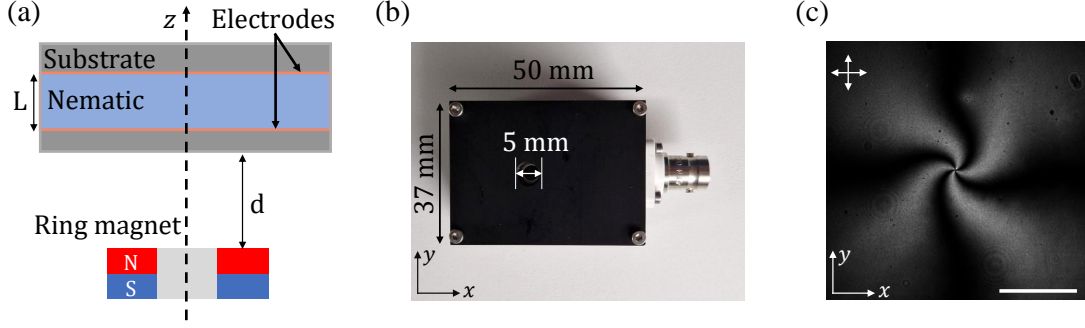


FIG. 1: (a) Side-view sketch of the spin-orbit liquid crystal device operated using the combined action of a uniform quasistatic electric field and a structured static magnetic field obtained from a ring magnet. (b) Top-view image of the device. (c) Observation of the topological structure of the nematic liquid crystal slab under an applied voltage of 4.70 V by optical imaging between crossed linear polarisers. Scale bar: 300 μm .

anisotropy at 100 kHz frequency.

As demonstrated in a previous work [30], under the combined action of magnetic and electric fields, a stable macroscopic topological defect with charge $q = +1$ spontaneously forms in the nematic, as shown in Fig. 1 (c). This defect behaves as an effective uniaxial slab with a tunable uniform birefringent phase retardation Δ , and an azimuthally varying optical axis orientated at an angle $\psi = q\varphi$ from the x -axis, where φ is the polar angle in the (x, y) plane. As a result, optical vortices with topological charges $l = \pm 2$ are generated for left- and right-circularly polarised incident Gaussian beams, provided that the phase retardation satisfies $\Delta = N\pi$, with N being an odd integer. In general, the device performs the following transformations:

$$|l, \sigma^\pm, \lambda\rangle \longrightarrow \left(\sqrt{1 - \eta_\lambda} |l, \sigma^\pm\rangle + \sqrt{\eta_\lambda} |l \pm 2, \sigma^\mp\rangle \right) |\lambda\rangle, \quad (1)$$

where σ^+ (σ^-) corresponds to the left (right)-circular polarisation states of wavelength λ , and $\eta_\lambda = \sin^2(\Delta/2)$ is the vortex conversion efficiency. The electric field allows us to tune Δ , hence the conversion efficiency, which enables control over the weights of the output light components. The vortex transformations also apply when a superposition of left- and right-circular polarisation is used

$$|l\rangle \left(\sqrt{\alpha} |\sigma^+\rangle + \sqrt{\beta} |\sigma^-\rangle \right) |\lambda\rangle \longrightarrow \left(\sqrt{1 - \eta_\lambda} \left(\sqrt{\alpha} |l, \sigma^+\rangle + \sqrt{\beta} |l, \sigma^-\rangle \right) + \sqrt{\eta_\lambda} \left(\sqrt{\alpha} |l + 2, \sigma^-\rangle + \sqrt{\beta} |l - 2, \sigma^+\rangle \right) \right) |\lambda\rangle, \quad (2)$$

where α and β represent the coefficients of the circularly polarised states.

This device, therefore, functions as an electrically tunable q-plate but distinguishes itself by its self-engineered nature. This enables both tuneable voltage features and high structural quality, in contrast to conventional q-plates, whether they are manufactured [24] or obtained via previous self-engineering strategies [23]. In particular, this allows manipulating more than one wavelength simultaneously, as already exploited in the context of optical imaging [28, 29]. For two input beams of wavelengths λ_1 and λ_2 , the output becomes

$$|l_1, \sigma^\pm, \lambda_1\rangle \otimes |l_2, \sigma^\pm, \lambda_2\rangle \longrightarrow \left(\sqrt{1 - \eta_{\lambda_1}} |l_1, \sigma^\pm\rangle + \sqrt{\eta_{\lambda_1}} |l_1 \pm 2, \sigma^\mp\rangle \right) |\lambda_1\rangle \otimes \left(\sqrt{1 - \eta_{\lambda_2}} |l_2, \sigma^\pm\rangle + \sqrt{\eta_{\lambda_2}} |l_2 \pm 2, \sigma^\mp\rangle \right) |\lambda_2\rangle, \quad (3)$$

Note that each respective efficiency η_λ depends uniquely only on the applied electric field, and Δ is wavelength-dependent. Hence, bimodal behaviour, i.e. two distinct topological charge output states, can be achieved by careful selection of the input states and the applied voltage, allowing spin-orbit coupling for individual colour modes simultaneously.

We now describe how this spin-orbit device is integrated with a nonlinear optical process. Anticipating the experiment to follow, we consider the case of a type-0 $\chi^{(2)}$ crystal where the only requirement is polarisation matching,

$\mathbf{e} + \mathbf{e} \rightarrow \mathbf{e}$. Here \mathbf{e} is a unit vector that denotes the polarisation state [31]. In this configuration, difference-frequency generation (DFG) occurs between two copolarised input fields at frequencies ω_1 and ω_2 , yielding a new frequency $\omega_{\text{DFG}} = \omega_1 - \omega_2$. In the context of structured light, the output electric field can be written as $\mathbf{E}_{\text{DFG}} \propto \mathbf{E}_1 \times \mathbf{E}_2^*$, where the complex conjugate introduces a phase difference that encodes the structure of both input fields. In bra-ket notation, the input state can be represented as a tensor product $|l_1, \sigma^\pm, \omega_1\rangle \otimes |l_2, \sigma^\pm, \omega_2\rangle$, and the resulting DFG output becomes

$$\mathbf{E}_{\text{DFG}} \equiv |l_1 - l_2, \mathbf{e}, \omega_1 - \omega_2\rangle \quad (4)$$

where the output polarisation \mathbf{e} aligns with the optical axis, which is fixed by the orientation of the anisotropic nonlinear crystal. When combined with the transformation rules of Eq. (3), it becomes clear that the device enables independent modulation of both wavelengths involved in the nonlinear interaction. The interplay between linear spin-orbit transformations and nonlinear selection rules thus creates new opportunities for both structuring light and probing structured light in nonlinear optical processes. We now turn to the experimental realisation of this concept.

III. EXPERIMENTAL SET-UP

The spin-orbit device was placed into the experimental setup shown in Fig. 2. A type-0 periodically poled KTP nonlinear crystal (NLC) was operated in DFG mode to generate an output beam of wavelength $\lambda_{\text{NIR}} = 808$ nm for input beams with wavelengths $\lambda_{\text{VIS}} = 532$ nm and $\lambda_{\text{IR}} = 1550$ nm. In this work, we target vortex conversion for wavelengths λ_{NIR} and λ_{IR} for which the device can be tuned electrically to operate on either a single wavelength or both simultaneously. The complex amplitude of the IR and VIS beams was controlled using two spatial light modulators (SLMs), SLM IR (Holoeye PLUTO) and SLM VIS (Holoeye GAEA 2), respectively. The VIS beam was collimated and expanded using a $4f$ system to overfill SLM VIS, while the Gaussian IR beam was simply collimated. The output from the two SLMs was relayed onto the front face of the NLC using telescopic $4f$ lens configurations. Half-wave plates (HWP) were used to align the polarisations for optimal phase matching. A dichroic mirror (DM) was used to overlap the two beams collinearly within the NLC. Finally, the DFG output was imaged into a single-mode fibre (SMF) and detected with an avalanche photodiode (APD) to perform an optical inner product measurement for modal decomposition [32]. In all experiments, a 100 kHz on/off voltage was applied to the spin-orbit device, and all voltages are quoted as root mean square values.

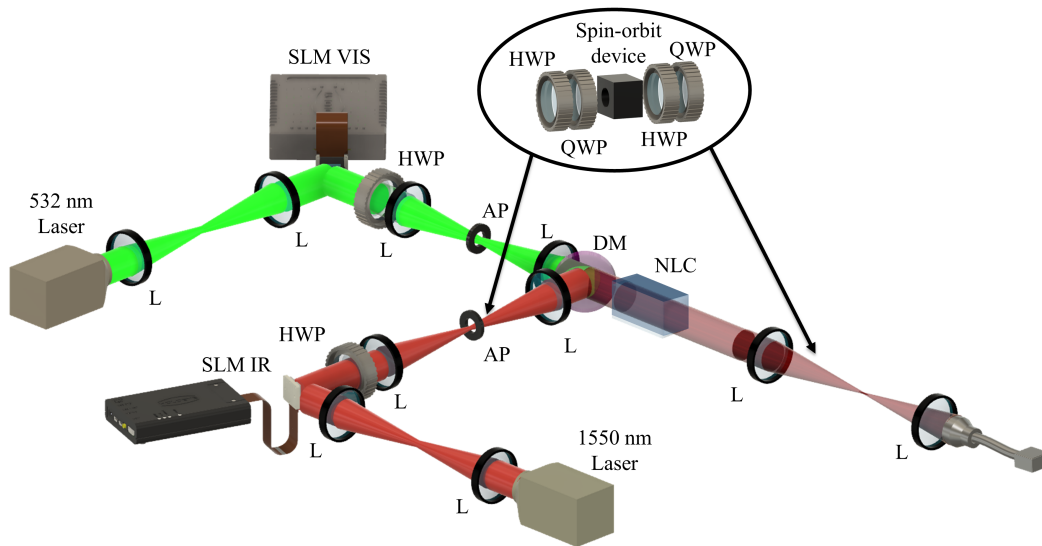


FIG. 2: Schematic of the experimental setup for nonlinear spatial mode detection with a spin-orbit device. A 532 nm (VIS) beam and a 1550 nm (IR) beam are expanded and collimated using a $4f$ -lens system before being modulated by spatial light modulators (SLM_{VIS} and SLM_{IR}). Half-wave plates (HWP) adjust the polarisation before the beams are combined in a nonlinear crystal (NLC) via a dichroic mirror (DM). The DFG process in the NLC produces an 808 nm (NIR) beam, whose spatial mode structure is analysed using a single-mode fibre (SMF) and an avalanche photodiode (APD). The inset shows that the spin-orbit device is placed either in the NIR or IR arm. HWPs and quarter-wave plates (QWP) control the ingoing and outgoing polarisation.

As shown in Fig. 2, the main experiment featured two configurations for the use of the spin-orbit device: in the first, the device was used *before* the crystal to modulate the $\lambda_{\text{IR}} = 1550$ nm, thereby altering the nonlinear interaction of the two input beams. In this configuration, the device acts as a shaping element, structuring the IR input to have OAM of l_{IR} . To test this efficacy, we use the VIS beam as a modal detector, exploiting the conjugate nature of the DFG process. Since the DFG output is coupled into a single-mode fibre (admitting only a Gaussian beam with $l_{\text{NIR}} = 0$), the selection rule for detection requires $l_{\text{IR}} = l_{\text{VIS}}$.

In the second configuration, the spin-orbit device was placed *after* the nonlinear crystal, and used to modulate the λ_{NIR} . Here the spin-orbit device (SOD) modifies the OAM of the DFG beam by adding an amount l_{SOD} to the output from the crystal. Thus, the final OAM becomes $l_{\text{NIR}} + l_{\text{SOD}}$, where $l_{\text{NIR}} = l_{\text{VIS}} - l_{\text{IR}}$ as a result of the nonlinear selection rule. Again, the output is coupled into a single-mode fibre to assess the performance via modal decomposition. These two configurations, combined with modal analysis as a performance metric, demonstrate that the device can both shape and detect structured light at two wavelengths, opening new avenues for nonlinear control and probing of complex light fields.

IV. RESULTS

We begin by characterising the device's efficiency, η_λ , as a function of applied voltage for the two wavelengths of interest in this study. To do so we measured the output power fraction, $P_\lambda^{\sigma^-}$, for input polarisation state σ^+ following $\eta_\lambda = P_\lambda^{\sigma^-} / (P_\lambda^{\sigma^+} + P_\lambda^{\sigma^-})$, with the results shown in Fig. 3. The results for wavelengths $\lambda_{\text{NIR}} = 808$ nm and $\lambda_{\text{IR}} = 1550$ nm demonstrate the tuneability of the conversion efficiency with applied voltage. In particular, an applied voltage of 4.70 V yields a maximal conversion efficiency of $\eta_{\lambda_{\text{IR}}} = 0.98$, whilst $\eta_{\lambda_{\text{NIR}}} = 0.03$ is minimised. These respective efficiencies allow for the creation of the bimodal state $|2, \sigma^-, \lambda_{\text{IR}}\rangle \otimes |0, \sigma^+, \lambda_{\text{NIR}}\rangle$. For $\eta_{\lambda_{\text{NIR}}}$, we observe maximal efficiencies of 0.99 and 0.98 at 3.75 V and 6.80 V applied voltage, respectively. At these applied voltages, $\eta_{\lambda_{\text{IR}}}$ is $\simeq 0.4$. Simultaneous efficiency optimisation for both wavelengths can be achieved at 4.04 V, with $\eta_{\lambda_{\text{NIR}}} = \eta_{\lambda_{\text{IR}}} = 0.72$, and at 5.89 V, with $\eta_{\lambda_{\text{NIR}}} = \eta_{\lambda_{\text{IR}}} = 0.79$.

Next, we characterised the modal performance of the device as a function of voltage, with the results shown in Fig. 4. We define modal purity in the OAM basis as the fractional power $|p_l|^2$ in the expansion $\sum p_l \exp(il\phi)$, where ϕ is the azimuthal angle, with the weights normalised so that $\sum |p_l|^2 = 1$. In the first experiment, the device is placed in the left-circularly polarised IR beam with SLM IR switched off, so that all the IR modulation is due to the spin-orbit device. In the second experiment, we keep SLM IR switched off and move the device to after the nonlinear crystal to modulate the DFG beam. In both cases, SLM VIS is programmed to produce $l_{\text{VIS}} \in \{-5, 5\}$ in the Laguerre-Gaussian basis by complex amplitude modulation and with no radial mode, i.e., $p = 0$ for all modes. The resulting detection into the single mode fibre ensures that the device's response can be uniquely determined by this modal analysis. The two set ups are schematically portrayed in the insets of Fig. 4 (a) and (b), respectively. The top panel in each plot shows the modal power in the expected $l = 2$ mode, $|p_2|^2$, with the bottom panels showing the full modal data, $|p_l|^2$, both as a function of voltage.

In agreement with the transformation rules in eq. (1), we see the spin-orbit device adds a topological charge of 2 for left circularly polarised input light. In Fig. 4 (a), since the device is placed before the crystal, detection is only possible when the OAM of the device and l_{VIS} match, here only when $l_{\text{VIS}} = 0$ or 2, tuned by the efficiency of the device. The highest modal purities were found to be $|p_2|^2 = 0.92 \pm 0.02$ at 4.70 V. Similar performance was found when the device modulated the DFG output beam, with the results shown in Fig. 4 (b). Now detection is only possible

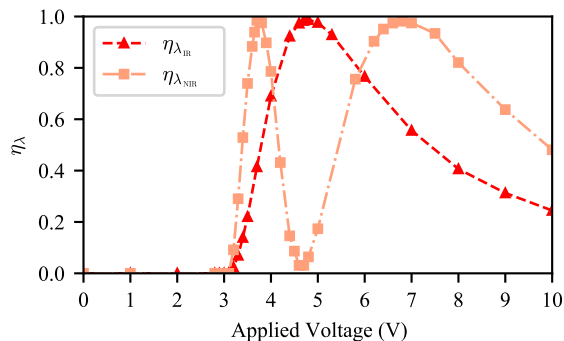


FIG. 3: Conversion efficiency, η_λ , as a function of applied voltage for $\lambda_{\text{NIR}} = 808$ nm and $\lambda_{\text{IR}} = 1550$ nm.

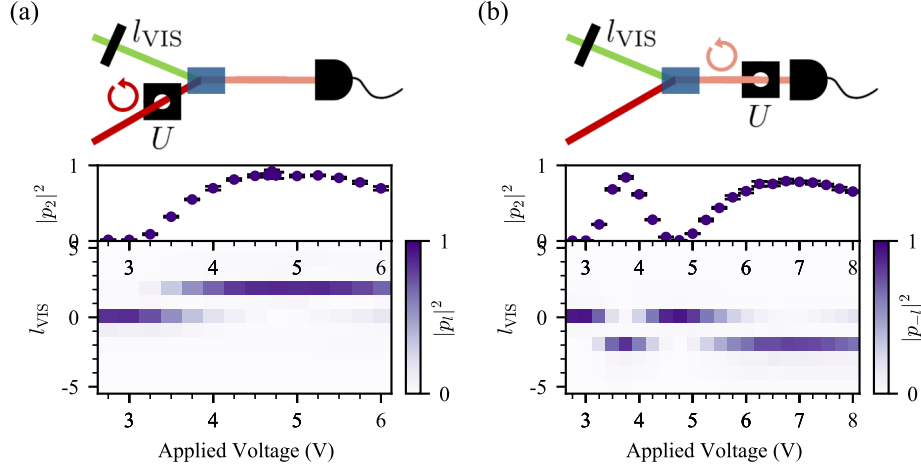


FIG. 4: Characterisation of the spin-orbit device as a function of applied voltage for wavelengths (a) 1550 nm and (b) 808 nm. Modal decomposition is illustrated in the bottom plots, showing the mean detection counts of 11 repeats for different $LG_{p=0, l}$ modes with l ranging from -5 to 5 prepared on SLM VIS. (a) Detection counts are maximised when l_{IR} after the device equals l_{VIS} . We observe that for a left-circularly polarised input beam, a topological charge of 2 is added by the device. (b) Here $l_{\text{NIR}} = l_{\text{VIS}}$, and detection counts are maximised when there is no OAM remaining in the NIR beam after the device. Again, we observe that for a left-circularly polarised input beam, a topological charge of 2 is added by the device. The top plots illustrate the modal purity of the $l = 2$ component after the spin-orbit device as a function of voltage. Highest modal purities were found to be (a) 0.92 ± 0.02 at 4.70 V and (b) 0.84 ± 0.02 at 3.75 V. The insets show the schematic setups for recording this data.

when the OAM of the device and l_{VIS} are conjugated, here only when $l_{\text{VIS}} = 0$ or -2 , tuned by the efficiency of the device. The highest modal purities were found to be $|p_2|^2 = 0.84 \pm 0.02$ at 3.75 V. The slightly lower purity when placing the device after the crystal may be due to aberrations and distortions introduced by the crystal itself.

We now study the performance in more detail only at these optimal voltages, performing modal decomposition for circularly and linearly polarised light incident on the spin-orbit device, as presented in Fig. 5 and Fig. 6. Once again, we show a schematic of the configuration in the inset to aid the reader. The IR shaping results are shown in Fig. 5. With the device switched off, Fig. 5 (a), only $l_{\text{IR}} = 0$ is detected. At the optimal voltage, changing the input polarisation alters the final state, clearly showing $l_{\text{IR}} = 2$ for left-circularly polarised light, and an equal weighting of $l_{\text{IR}} = \pm 2$ for linearly polarised light, as seen in Figs. 5 (b) and (c), respectively. The low contributions from other

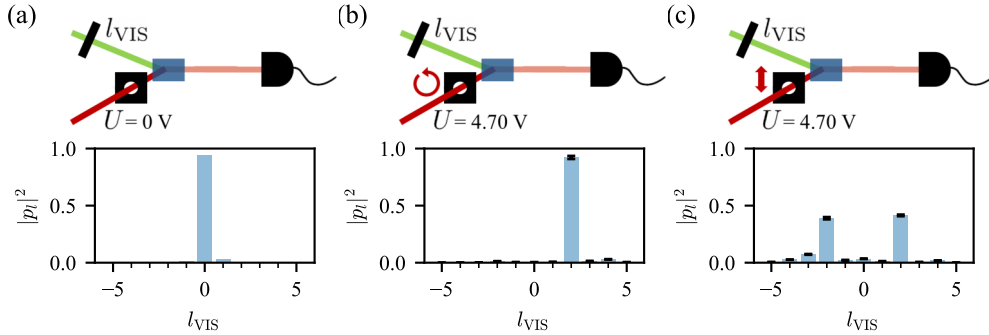


FIG. 5: Modal decomposition with the spin-orbit coupling in the 1550 nm arm of the nonlinear system. Detection counts are maximised when $l_{\text{IR}} = l_{\text{VIS}}$. Error bars show the standard deviation of 11 repeats for a 1 s measurement time. (a) Without an applied voltage, the spin-orbit coupling leaves the $l_{\text{IR}} = 0$ OAM value unaltered. When the optimal IR voltage of 4.70 V is applied, we observe the spin-orbit device converts $l_{\text{IR}} = 0$ to (b) $l_{\text{IR}} = 2$ for incident left circularly polarised light and (c) an equal superposition of $l_{\text{IR}} = \{-2, 2\}$ for linearly polarised incident light.

The insets show the schematic setups for recording this data.

OAM subspaces are evident on the bar graphs.

Fig. 6 shows the full modal spectrum when the two input beams, VIS and IR, are shaped by SLMs and the DFG is shaped by the spin-orbit device. When the device is turned off, Fig. 6 (a), the result is a cross-talk matrix with only a diagonal signal, highlighted in red for visualisation. When the device is turned on, the functionality depends on the voltage, incoming polarisation and wavelength. Now we modulate the NIR beam at the optimal voltage for two incoming polarisations, left-circular and linear, with the results shown in Figs. 6 (b) and (c). We observe an addition of topological charge 2 for left circularly polarised light, evident by the shift of the diagonal counts by +2. For incident linearly polarised light, the spin-orbit device both adds and subtracts a topological charge of 2 to the input mode, resulting in a dual offset in the diagonal. The original state is shown in red for visualisation. The slightly lower counts for the downshifted curve might be due to alignment or small polarisation mismatch.

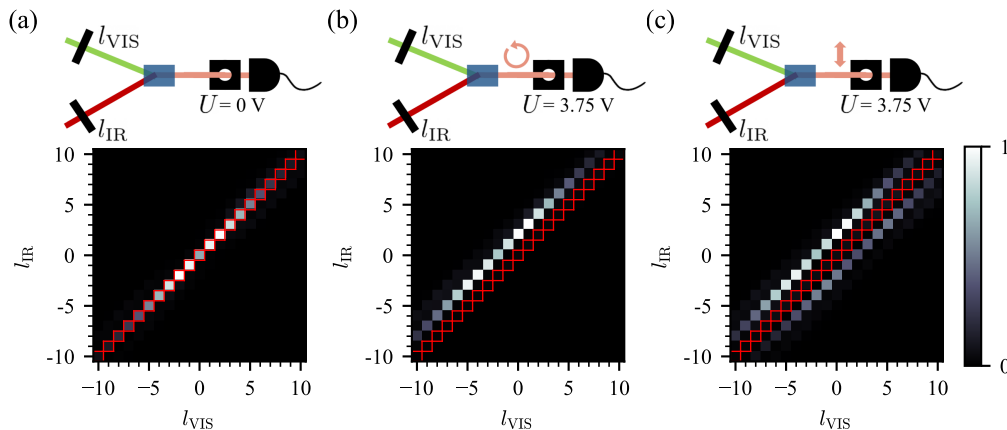


FIG. 6: Modal decomposition with the spin-orbit device in the 808 nm arm of the nonlinear system. After the crystal, $l_{\text{NIR}} = l_{\text{VIS}} - l_{\text{IR}}$. When $l_{\text{NIR}} = 0$ after the device, maximal counts are detected. (a) Without an applied voltage, the spin-orbit coupling leaves the l_{NIR} unaltered. When the optimal NIR voltage of 3.75 V is applied, we observe the device adds a topological charge of (b) 2 for incident left circular light and (c) an equal superposition of 2 and -2 for incident linear light. We infer these OAM conversions from the diagonal shifts of maximal detection events in the modal decomposition. The red square outlines indicate when $l_{\text{VIS}} = l_{\text{IR}}$. The insets show the schematic set ups for recording this data.

V. CONCLUSION

We exploited a wavelength-tunable spin-orbit device that flips the helicity of circularly polarised input light and changes its OAM state by amounts of two units, in a nonlinear optics framework. This is achieved by a stable topological defect in a nematic slab that results from the combined action of magnetic and electric fields. We show this device can perform spin-orbit coupling for 1550 nm with efficiency $\eta_{\lambda_{\text{IR}}} = 0.98$ but leaves 808 nm unaffected ($\eta_{\lambda_{\text{NIR}}} = 0.03$). This enables the generation of a bimodal state that is wavelength-dependent. Additionally, both wavelengths can be subjected to spin-orbit coupling simultaneously. We reported an efficiency $\eta_{\lambda}(U)$ look-up table that reports how their respective efficiencies depend on the applied electric field. For 808 nm, we can achieve maximum efficiency $\eta_{\lambda_{\text{NIR}}} = 0.99$ ($\eta_{\lambda_{\text{IR}}} \simeq 0.4$). The maximum efficiency for bi-colour spin-orbit coupling was found $\eta_{\lambda_{\text{NIR}}} = \eta_{\lambda_{\text{IR}}} = 0.79$.

Summarising, we characterised how a spin-orbit device can affect the modal purity of an input OAM spectrum for λ_{IR} and λ_{NIR} in a nonlinear DFG process such that modal decomposition measurements were performed exclusively in the more easily accessible NIR spectral range. The modal purity of generated OAM mode as a function of the applied voltage exhibited a response mirroring η_{λ} , which quantifies the power fraction of an incident circularly polarised component that is processed by the spin-orbit interaction. High-purity OAM conversions by the spin-orbit device at the voltage values corresponding to maximal efficiency were observed for both circularly and linearly polarised input light, in agreement with theoretical predictions. These results highlight that a wavelength-tunable spin-orbit device opens the door for a wide range of applications in structured light and quantum information. In particular, the superposition coefficients of hybrid states $|l, e, \lambda\rangle$ can be precisely controlled. Furthermore, output bimodal states can be generated with extremely high efficiencies.

VI. ACKNOWLEDGEMENTS

The authors would like to thank the CNRS-Wits collaboration fund.

-
- [1] Forbes A, de Oliveira M and Dennis M R 2021 *Nature Photonics* **15** 253–262
 - [2] Yang Y, Forbes A and Cao L 2023 *Opto-Electronic Science* **2** 230026–1
 - [3] Dorrah A H and Capasso F 2022 *Science* **376** eabi6860
 - [4] Angelsky O V, Bekshaev A Y, Hanson S G, Zenkova C Y, Mokhun I I and Zheng J 2020 *Frontiers in Physics* **8** 114
 - [5] Wang J and Liang Y 2021 *Frontiers in Physics* **9** 688284
 - [6] Buono W T and Forbes A 2022 *Opto-Electronic Advances* **5** 210174–1
 - [7] Li G, Zhang S and Zentgraf T 2017 *Nature Reviews Materials* **2** 1–14
 - [8] Sephton B, Vallés A, Nape I, Cox M A, Steinlechner F, Konrad T, Torres J P, Roux F S and Forbes A 2023 *Nature communications* **14** 8243
 - [9] Qiu X, Guo H and Chen L 2023 *Nature Communications* **14** 8244
 - [10] Xu Y, Tang S, Nicholas Black A and Boyd R W 2023 *Optics Express* **31** 42723–42729
 - [11] Singh S, Sephton B, Tavares Buono W, D’Ambrosio V, Konrad T and Forbes A 2024 *Advanced Photonics* **6** 026003–026003
 - [12] Ackermann L, Roider C, Cvecek K, Barré N, Aigner C and Schmidt M 2023 *Scientific Reports* **13** 10338
 - [13] Liu S, Mazur L M, Krolikowski W and Sheng Y 2020 *Laser & Photonics Reviews* **14** 2000224
 - [14] da Silva B P, dos Santos G, de Oliveira A, da Silva N R, Buono W, Gomes R, Soares W, Jesus-Silva A, Fonseca E, Ribeiro P S et al. 2022 *Optica* **9** 908–912
 - [15] Abrahao R A, Morin H P, Pagé J T, Safari A, Boyd R W and Lundeen J S 2024 *Optica* **11** 1549–1555
 - [16] Wu H J, Yang H R, Rosales-Guzmán C, Gao W, Shi B S and Zhu Z H 2019 *Physical Review A* **100** 053840
 - [17] Wu H J, Yu B S, Zhu Z H, Gao W, Ding D S, Zhou Z Y, Hu X P, Rosales-Guzmán C, Shen Y and Shi B S 2022 *Optica* **9** 187–196
 - [18] Shen Y, Zhang Q, Shi P, Du L, Yuan X and Zayats A V 2024 *Nature Photonics* **18** 15–25
 - [19] Zhan Q 2024 *Advances in Optics and Photonics* **16** 163–228
 - [20] Shen Y and Rosales-Guzmán C 2022 *Laser & Photonics Reviews* **16** 2100533
 - [21] Bliokh K Y, Rodríguez-Fortuño F J, Nori F and Zayats A V 2015 *Nature Photonics* **9** 796–808
 - [22] Cardano F and Marrucci L 2015 *Nature Photonics* **9** 776–778
 - [23] Barboza R, Bortolozzo U, Clerc M, Residori S and Vidal-Henriquez E 2015 *Advances in Optics and Photonics* **7** 635–683
 - [24] Rubano A, Cardano F, Piccirillo B and Marrucci L 2019 *Journal of the optical society of america B* **36** D70–D87
 - [25] Hakobyan V and Brasselet E 2025 *Physical Review Letters* **134** 083802
 - [26] Kopf L, Barros R and Fickler R 2023 *ACS Photonics* **11** 241–246
 - [27] Liu X, Cao Q and Zhan Q 2024 *Photonics Insights* **3** R08–R08
 - [28] Yan L, Gregg P, Karimi E, Rubano A, Marrucci L, Boyd R and Ramachandran S 2015 *Optica* **2** 900–903
 - [29] Arjmand P, Thodika S C, Li H, Bivas E, Oheim M, Yoshida H, Brasselet E and Guillon M 2025 *ACS Photonics* **12** 648–654
 - [30] Brasselet E 2018 *Physical review letters* **121** 033901
 - [31] Manjooran S, Zhao H, Lima I and Major A 2012 *Laser Physics* **22** 1325–1330
 - [32] Pinnell J, Nape I, Sephton B, Cox M A, Rodríguez-Fajardo V and Forbes A 2020 *JOSA A* **37** C146–C160